

# Forecasting Long-Lived Lagrangian Vortices from their Objective Eulerian Footprints

Mattia Serra\* and George Haller†

Institute for Mechanical Systems, ETH Zürich  
Leonhardstrasse 21, 8092 Zurich, Switzerland

November 8, 2018

## Abstract

We derive a non-dimensional metric to quantify the expected Lagrangian persistence of objectively defined Eulerian vortices in two-dimensional unsteady flows. This persistence metric is the averaged deviation of the vorticity from its spatial mean over the Eulerian vortex, normalized by the instantaneous material leakage from the Eulerian vortex. The metric offers a model- and frame-independent tool for uncovering the instantaneous Eulerian signature of long-lived Lagrangian vortices. Using satellite-derived ocean velocity data, we show that Lagrangian vortex-persistence predictions by our metric significantly outperform those inferred from other customary Eulerian diagnostics, such as the potential vorticity gradient and the Okubo-Weiss criterion.

## 1 Introduction

Coherent Lagrangian vortices (Haller, 2015) are fluid masses enclosed by material boundaries that exhibit only moderate deformation under advection. Such vortices play a fundamental role in a number of transport and mixing processes. For instance, coherent mesoscale oceanic eddies are known to carry water over long distances, influencing global circulation and climate (Beal et al., 2011).

Frame-invariant methods for the precise identification of coherent Lagrangian vortex boundaries are now available (Haller and Beron-Vera, 2013; Farazmand and Haller, 2016; Haller et al., 2016). These methods, as any Lagrangian approach, are intrinsically tied to a preselected finite time interval. Some material vortex boundaries lose their coherence immediately beyond their extraction times, while others remain coherent over much longer intervals (Haller and Beron-Vera, 2013; Beron-Vera et al., 2013; Wang et al., 2016). It is, therefore, of interest to identify a signature of long-lived Lagrangian vortices without an a priori knowledge of their time scale of existence.

The question we address in the present paper is the following: What instantaneous Eulerian features of a coherent Lagrangian vortex make it likely to persist over longer time intervals? This question is relevant, for instance, in environmental forecasting and decision-making, as well as in assessing the life stage of coherent eddies that influence the general circulation in the ocean. Despite its importance, however, the question of Lagrangian vortex persistence has received little attention. Broadly used Eulerian vortex detection methods provide no direct answer, although the motivation

---

\*serram@ethz.ch

†Email address for correspondence: georgehaller@ethz.ch

for these Eulerian methods is often precisely the need to capture sustained material transport by vortices. Clearly, the future of advected water masses in an unsteady flow cannot be precisely predicted based on just present data. Reasons for this include unforeseeable future interactions with other vortices, and a priori unknown external forcing on the flow. The most one can hope for, therefore, is to forecast Lagrangian eddy persistence, with high enough probability, assuming that these unpredictable effects do not arise.

To this end, we propose here a non-dimensional metric to assess the persistence of Eulerian vortices encircled by elliptic Objective Eulerian Coherent Structures (OECSs), as defined by Serra and Haller (2016). Such OECSs are closed curves with no short-term unevenness in their material deformation rates (zero short-term filamentation). The objectivity of OECSs ensures the frame-invariance of the transport estimates they provide, while the non-dimensionality of the persistence metric introduced here will allow for a comparison of coexisting vortices of various sizes and times scales.

Our persistence metric is the ratio of the rotational coherence strength of an elliptic OECS to its material leakage. Eulerian vortices with high rotation rates and low material leakage will have high persistence metric values and will be seen to delineate regions of sustained material coherence. As a side result, we also derive an explicit formula for the material flux through an elliptic OECS. This technical result is generally applicable to estimating the deformation of limit cycles in a two-dimensional vector field under a change in the system parameters.

We illustrate our results on an unsteady satellite altimetry-based velocity field of the South Atlantic Ocean. Remarkably, we find that elliptic OECSs with high values of the persistence metric capture, with high probability, the signature of long-lived Lagrangian vortices. At the same time, the predictive power of customary Eulerian diagnostics, such as the Okubo-Weiss (*OW*) criterion (Okubo, 1970; Weiss, 1991), the potential vorticity (*PV*) and the potential vorticity gradient ( $\nabla PV$ ) (Griffa et al., 2007), turns out to be substantially lower, showing correlations below 0.5 with the actual lifetime of Lagrangian eddies.

## 2 Set-up and notation

We consider an unsteady velocity field  $v(x, t)$  defined on a spatial domain  $U \subset \mathbb{R}^2$  over a finite time interval  $[t_0, t_1]$ . We recall the velocity gradient decomposition

$$\nabla v(x, t) = S(x, t) + W(x, t), \quad (1)$$

where  $S = \frac{1}{2}(\nabla v + \nabla v^\top)$  and  $W = \frac{1}{2}(\nabla v - \nabla v^\top)$  are the rate-of-strain tensor and the spin tensor, respectively.

The spin tensor  $W$  is skew-symmetric while  $S$  is symmetric, with its eigenvalues  $s_i(x)$  and eigenvectors  $e_i(x)$  satisfying

$$e_2 S e_i = s_i e_i, \quad |e_i| = 1, \quad i = 1, 2; \quad s_1 \leq s_2, \quad e_2 = R e_1 = \begin{bmatrix} 0 & -1 \\ 1 & 0 \end{bmatrix} e_1.$$

Fluid particle trajectories generated by  $v(x, t)$  are solutions of the differential equation  $\dot{x} = v(x, t)$ , defining the flow map

$$F_{t_0}^t(x_0) = x(t; t_0, x_0), \quad x_0 \in U, \quad t \in [t_0, t_1],$$

which maps initial particle positions  $x_0$  at time  $t_0$  to their time- $t$  positions,  $x(t; t_0, x_0)$ .

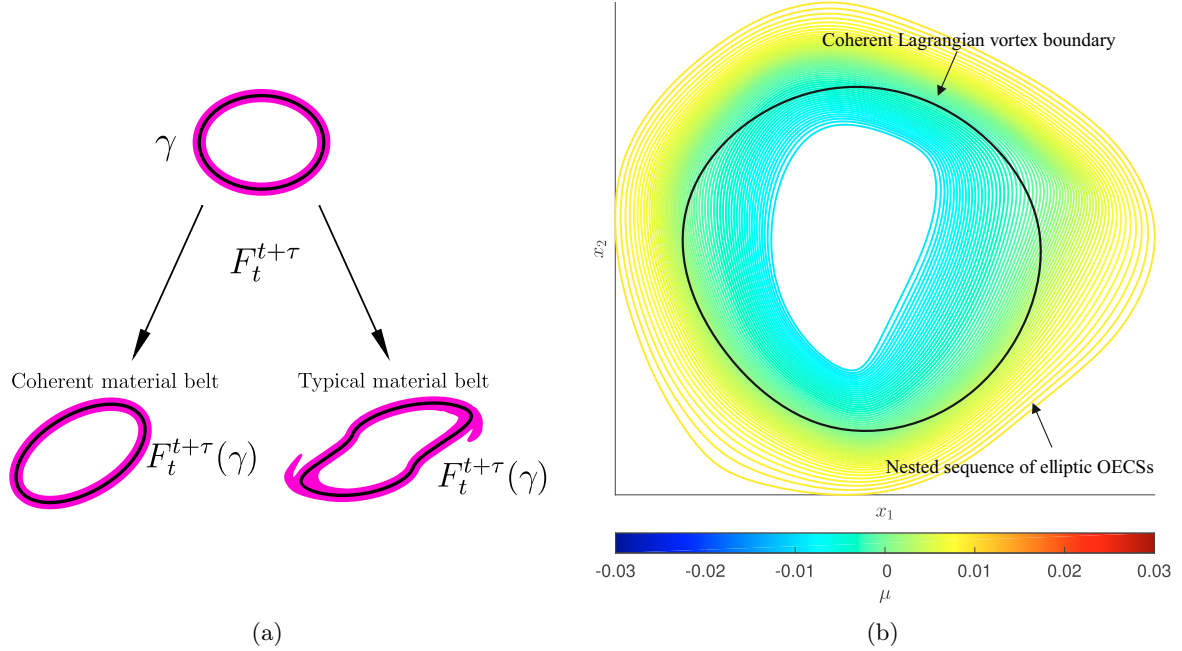


Figure 1: (a) A closed material curve  $\gamma$  (black) at time  $t$  is advected by the flow into its later position  $F_t^{t+\tau}(\gamma)$ , with  $\tau \approx 0$ . The advected curve remains coherent if an initially uniform material belt (magenta) around it shows no leading-order variations in stretching rate. (b) Nested family of elliptic OECSs in a flow example, analyzed in more detail in section 6, for different values of  $\mu$  (in color). The elliptic OECS family fills a region that also turns out to contain a persistent Lagrangian vortex in this example (Haller and Beron-Vera, 2013).

### 3 Vortices as elliptic OECSs

A typical set of fluid particles is subject to significant stretching under advection in an unsteady flow. Even in the limit of zero advection time, fluid elements generally experience considerable stretching rates. One may look for the Eulerian signatures of coherent material vortices as exceptional sets of fluid trajectories that defy this general trend. Specifically, Serra and Haller (2016) seek boundaries of Eulerian coherent vortices as closed instantaneous curves across which the averaged material stretching rate shows no leading-order variability.

Mathematically, this is equivalent to seeking closed curves  $\gamma$  whose  $\mathcal{O}(\epsilon)$  perturbations show no  $\mathcal{O}(\epsilon)$  variability in the averaged strain-rate functional  $\dot{Q}_t(\gamma)$ , defined as

$$\dot{Q}_t(\gamma) = \frac{1}{\sigma} \oint_{\gamma} \frac{\langle x'(s), S(x(s), t) x'(s) \rangle}{\langle x'(s), x'(s) \rangle} ds.$$

Here  $x(s)$ ,  $s \in [0, \sigma]$ , denotes the arclength parametrization of  $\gamma$  at time  $t$ , and  $x'(s)$  denotes its local tangent vector. Stationary curves of  $\dot{Q}_t(\gamma)$  are cores of exceptional material belts showing perfect short-term coherence (Fig. 1a). Serra and Haller (2016) show that closed stationary curves of  $\dot{Q}_t(\gamma)$  are precisely the closed null-geodesics of a suitably defined Lorentzian metric. Along these curves, the tangential stretching rate  $\mu$  is constant.

The closed stationary curves of  $\dot{Q}_t(\gamma)$  turn out to be computable as limit cycles of the direction field family

$$x' = \chi_{\mu}^{\pm}(x), \quad \chi_{\mu}^{\pm}(x) = \sqrt{\frac{s_2(x) - \mu}{s_2(x) - s_1(x)}} e_1(x) \pm \sqrt{\frac{\mu - s_1(x)}{s_2(x) - s_1(x)}} e_2(x), \quad (2)$$

within the domain  $U_\mu \subset U$  defined as

$$U_\mu = \{x \in U \mid s_2 - s_1 \neq 0, s_1 \leq \mu \leq s_2\}.$$

The direction field family (2) depends on the choice of the sign parameter  $\pm$ , as well as on the parameter  $\mu \in \mathbb{R}$ . We define elliptic OECSs as limit cycles of (2) for each value of the parameter  $\mu \approx 0$ . The  $\mu = 0$  member of this one-parameter family of nested curves represents a perfect instantaneously coherent vortex boundary (Serra and Haller, 2016). Such a closed curve is highly atypical, exhibiting no instantaneous stretching rate.

Members of limit cycles families of  $\chi_\mu^\pm$  cannot intersect. Each limit cycle either grows or shrinks under changes in  $\mu$ , forming a smooth annular belt of non-intersecting loops (see Serra and Haller (2016) for details). This annular Eulerian belt often surrounds a persistent Lagrangian vortex boundary, as in the example shown in Fig. 1b.

## 4 Material flux through elliptic OECSs

In this section, we derive an explicit formula for the material flux through an elliptic OECS to quantify the degree to which the OECS is Lagrangian. As a byproduct, we obtain an expression for the short-term continuation of elliptic OECSs under varying time.

Let  $\gamma(t)$  be a time-varying, closed curve family parametrized by a function  $x(s, t)$ . The pointwise instantaneous material flux density through  $\gamma(t)$  is then given by

$$\begin{aligned} \varphi(x(s, t), t) &= \langle v(x(s, t), t) - \frac{d}{dt}x(s, t), n(x(s, t), t) \rangle \\ &= \langle v(x(s, t), t), n(x(s, t), t) \rangle - \left[ \frac{d}{dt}x(s, t) \right]^\perp, \end{aligned} \quad (3)$$

i.e., by the curve-normal projection  $\langle \cdot, n(x(s, t), t) \rangle$  of the Lagrangian velocity  $v(x(s, t), t)$  of a trajectory relative to the velocity of  $\gamma(t)$ .

In our context,  $x(s, t)$  represents a limit cycle of the ODE (2), thus we have  $n(x(s, t), t) = [\chi_\mu^\pm(x(s, t), t)]^\perp = R\chi_\mu^\pm(x(s, t), t)$ . In Appendix A, we derive and solve an ODE for the unknown term  $\left[ \frac{d}{dt}x(s, t) \right]^\perp$  in (3), obtaining the final formula

$$\left[ \frac{d}{dt}x(s, t) \right]^\perp = \Phi_0^s(t) \left[ \frac{d}{dt}x(0, t) \right]^\perp + \Pi(s, t), \quad \Pi(s, t) := \Phi_0^s(t) \int_0^s (\Phi_0^\vartheta(t))^{-1} \tilde{c}(\vartheta, t) d\vartheta, \quad (4)$$

with  $\Phi_0^s(t)$  denoting the matrix

$$\Phi_0^s(t) = \begin{bmatrix} 1 & \int_0^s e^{\int_0^\vartheta \nabla \cdot \chi_\mu^\pm(x(\vartheta, t), t) d\vartheta} \kappa(x(\vartheta, t)) d\vartheta \\ 0 & e^{\int_0^s \nabla \cdot \chi_\mu^\pm(x(\vartheta, t), t) d\vartheta} \end{bmatrix}, \quad (5)$$

and

$$\begin{aligned} \tilde{c}(s, t) &= [0, \psi(x(s, t), t)]^\top, \\ \psi(x(s, t), t) &= \frac{-\langle \chi_\mu^\pm(s, t), \partial_t S(s, t) \chi_\mu^\pm(s, t) \rangle}{2\langle \chi_\mu^\pm(s, t), S(s, t) \chi_\mu^\pm(s, t)^\perp \rangle}, \\ \kappa(x(s, t)) &= \langle \nabla \chi_\mu^\pm(s, t) \chi_\mu^\pm(s, t), R\chi_\mu^\pm(s, t) \rangle. \end{aligned} \quad (6)$$

Note that  $\kappa$  represents the pointwise curvature along the elliptic OECS with respect to the normal vector defined as  $[\chi_\mu^\pm]^\perp = R\chi_\mu^\pm$ .

In Appendix A, we also derive the following equation for the correct initial condition of  $\left[ \frac{d}{dt}x(s, t) \right]^\perp$ :

$$\left[ \frac{d}{dt}x(0, t) \right]^\perp = \frac{\langle \Pi(0, t), d \rangle}{1 - \rho_2(t)}, \quad \rho_2(t) = e^{\int_0^t \nabla \cdot \chi_\mu^\pm(x(\vartheta, t), t) d\vartheta}, \quad d := \begin{bmatrix} 0 \\ 1 \end{bmatrix}. \quad (7)$$



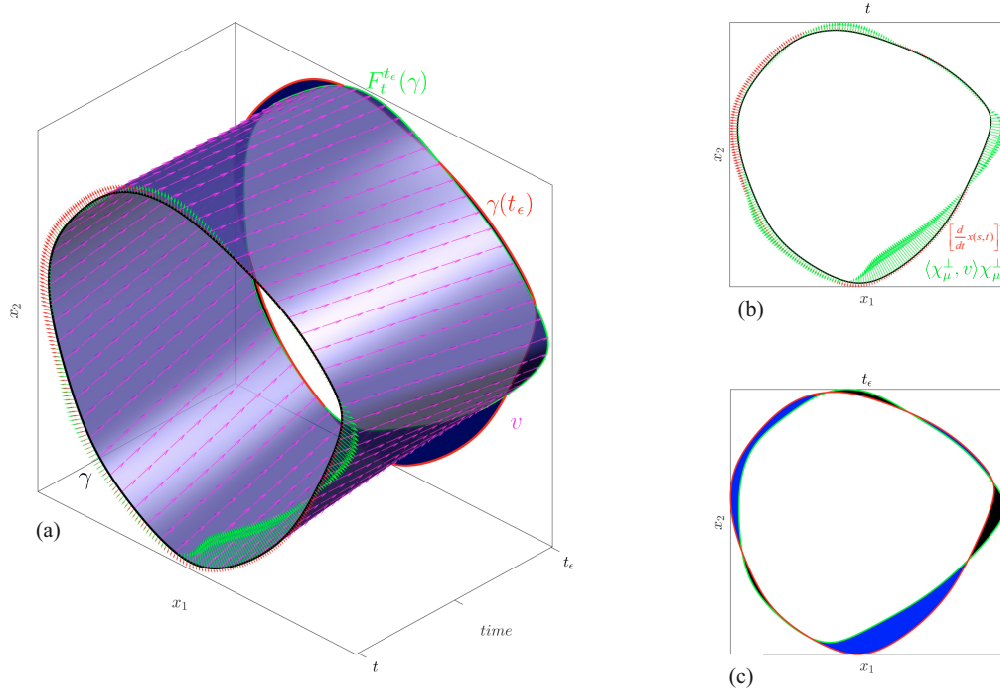


Figure 2: (a) Initial elliptic OECS  $\gamma$  (black) and its advected image under the flow in the extended phase space over  $[t, t_\epsilon]$ , where  $t_\epsilon = t + \epsilon\Delta t$ . At time  $t$ , the flow velocity perpendicular to the curve and the corresponding elliptic OECS velocity are reported by the green and red arrows, respectively. At time  $t_\epsilon$ , the advected image,  $F_t^{t_\epsilon}(\gamma)$ , is shown in green while the recomputed elliptic OECS  $\gamma(t_\epsilon)$  in red. (b) Slice of (a) at time  $t$ . (c) Slice of (a) at time  $t_\epsilon$ . The blue and black areas represent the actual inward and outward material flux across  $\gamma$  over  $[t, t_\epsilon]$ , respectively.

This initial condition represents the ratio between the magnitude of the perturbation needed to destroy the limit cycle due to the unsteadiness of the flow and the strength of the hyperbolicity of the limit cycle. For steady flows, we have  $\Pi^\perp(s, t) = 0$  since  $\tilde{c}(s, t) = 0$ . In that case, the robustness of the limit cycle is determined by  $\rho_2(t) \equiv \rho_2 = \text{const.}$ , without any time dependence.

For the computation of  $\partial_t S$  in (6), we employ a backward finite-difference scheme (see Appendix C for details). Once  $[\frac{d}{dt}x(0, t)]^\perp$  is known, we evaluate the pointwise flux density introduced in (3). For a counterclockwise parametrization of  $\gamma(t)$ , and for our definition of  $[\chi_\mu^\pm]^\perp$ , positive values of  $\varphi(x(s, t), t)$  represents inward material flux.

Figure 2a illustrates an elliptic OECS  $\gamma(t)$  (black) at time  $t$ , for a fixed value of  $\mu$ , with its advected image over the time window  $[t, t_\epsilon]$  in the extended phase space of position and time. Figures 2a-b show the initial and final time slices of Fig. 2a. The materially advected image of  $\gamma$  at time  $t_\epsilon$ ,  $F_t^{t_\epsilon}(\gamma)$ , is shown in green while the elliptic OECS  $\gamma(t_\epsilon)$  computed at time  $t_\epsilon$ , is shown in red. Figures 2 a-b show the instantaneous pointwise material flux density through  $\gamma(t)$ , given by the difference between the flow velocity normal to the curve (green arrows) and the corresponding continuation velocity (red arrows). Given formula (3), the total instantaneous material flux across  $\gamma(t)$  is

$$\varphi_{\gamma(t)} = \oint_{\gamma(t)} \varphi(x(s, t), t) ds,$$

with

$$\begin{cases} \varphi(x(s, t), t) = \langle v(x(s, t), t), [\chi_\mu^\pm]^\perp(x(s, t), t) \rangle - \langle \Phi_0^s(t) [\frac{d}{dt}x(0, t)]^\perp + \Pi(s, t), d \rangle, \\ [\frac{d}{dt}x(0, t)]^\perp = \frac{\langle \Pi(\sigma, t), d \rangle}{1 - e^{\int_0^\sigma \nabla \cdot \chi_\mu^\pm(x(\vartheta, t), t) d\vartheta}}. \end{cases}$$

The instantaneous total material flux  $\varphi_{\gamma(t)}$ , multiplied by  $\epsilon\Delta t$ , approximates the actual material flux given by the inward (blue) area minus the outward (black) area shown in Fig. 2c.

## 5 Persistence metric for elliptic OECSs

We now propose a non-dimensional objective metric that classifies elliptic OECSs based on their expected persistence in time. We first define the two ingredients needed for this metric: the *rotational coherence* and the *relative material leakage*.

**Definition 1.** The rotational coherence of an elliptic OECS  $\gamma(t)$  is

$$\omega_\gamma(t) := \frac{|\int_{A_{\gamma(t)}} [\omega(x, t) - \bar{\omega}(t)] dA|}{A_{\gamma(t)}}, \quad (8)$$

where  $\omega(x, t)$  denotes the vorticity,  $A_{\gamma(t)}$  is the area enclosed by  $\gamma(t)$ , and

$$\bar{\omega}(t) = \frac{\int_{A_{\partial U}} \omega(x, t) dA}{A_{\partial U}}$$

is the mean spatial vorticity over the domain  $U$  with boundary  $\partial U$ .

The rotational coherence  $\omega_\gamma$  represents the normed mean vorticity deviation within  $\gamma(t)$ , inspired by related quantities defined in Haller et al. (2016). Specifically, the rotational coherence measures the strength of a vortical structure arising from its rotational speed. The classic measure of vortex strength, also called circulation (Batchelor, 2000), relies solely on the vorticity  $\omega(x, t)$ , and is therefore frame-dependent. The rotational coherence  $\omega_\gamma$ , instead, involves the vorticity deviation, which is frame-independent (Appendix B). Elliptic OECSs with high rotational coherence are shielded by locally high levels of shear, and hence are expected to persist in time.

**Definition 2.** The relative material leakage of an elliptic OECSs  $\gamma(t)$  is

$$\Gamma_\gamma(t) := \frac{\oint_{\gamma(t)} |\varphi(x(s, t), t)| ds}{A_{\gamma(t)}}. \quad (9)$$

The relative material leakage measures the rate of material area leaking out of  $\gamma(t)$  due to its non-Lagrangian evolution, divided by the initial area of  $\gamma(t)$ . A  $\gamma(t)$  with low  $\Gamma_\gamma(t)$  identifies an exceptional curve that exhibits low inhomogeneity in its stretching rates both in its initial position and in its short-term advected position. The absolute value in (9) prevents the cancellation of opposite-sign material flux contributions. Note that both  $\omega_\gamma$  and  $\Gamma_\gamma$  have the dimension  $[time^{-1}]$ .

We expect elliptic OECSs with high rotational coherence and low material leakage to be the best candidate locations for Lagrangian vortices. To this end, we define the *persistence metric* of an elliptic OECS as the following objective, non-dimensional quantity:

**Definition 3.** The persistence metric of elliptic OECS  $\gamma(t)$  is

$$\Theta_\gamma(t) := \frac{\text{rotational coherence}}{\text{relative material leakage}} = \frac{\omega_\gamma(t)}{\Gamma_\gamma(t)} = \frac{|\int_{A_{\gamma(t)}} [\omega(x, t) - \bar{\omega}(t)] dA|}{\oint_{\gamma(t)} |\varphi(x(s, t), t)| ds}. \quad (10)$$

The non-dimensional nature of  $\Theta_\gamma$  is immediate from equation (10), while its frame-invariance follows from the objectivity of the scalar quantities involved in its definition (cf. Appendix B). The non-dimensionality of  $\Theta_\gamma$  allows us to characterize the persistence of vortices regardless of their spatial and temporal scales, which are often abundant and unknown. The objectivity of  $\Theta_\gamma$  ensures a persistence assessment independent of the frame of reference.

In case of zero relative material leakage, we have  $\Theta_\gamma = \infty$ , as indeed desired for a perfectly material elliptic OECSs. In this rare case,  $F_t^{t_\epsilon}(\gamma(t)) = \gamma(t_\epsilon)$  and hence the green and the red curves in Fig. 2c coincide.

In Appendix C, we summarize the numerical algorithms for the identification of likely long-lived Lagrangian vortices from their objective Eulerian features. Specifically, Algorithm 1 summarizes the computation of elliptic OECSs and Algorithm 2 describes the computation of the corresponding persistence metric  $\Theta_\gamma$ .

## 6 Example: Forecasting persistent Lagrangian vortices in satellite-derived ocean velocity data

We apply our OECS-based vortex-coherence forecasting scheme to a two-dimensional unsteady ocean dataset obtained from AVISO satellite altimetry measurements (<http://www.aviso.oceanobs.com>). The domain of interest is the Agulhas leakage in the Southern Atlantic Ocean bounded by longitudes  $[17^\circ W, 7^\circ E]$  and latitudes  $[38^\circ S, 22^\circ S]$ . The Agulhas Current is a narrow western boundary current of the southwest Indian Ocean, whose interaction with the strong Antarctic Circumpolar Current gives rise to Agulhas rings, the largest mesoscale eddies in the ocean.

Agulhas rings are considered important in the global circulation due to the large amount of water they carry over considerable distances (Beal et al., 2011). For comparison with earlier Lagrangian analysis (Haller and Beron-Vera, 2013), we consider the same initial time  $t = 24$  November 2006 and a similar but slightly larger spatial domain. For more detail on the dataset and the numerical method, see Appendix C and Appendix D.

As mentioned earlier, the  $OW$  parameter

$$OW(x, t) = s_2^2(x, t) - \omega^2(x, t),$$

is a frequently used indicator of instantaneous ellipticity in unsteady fluid flows (Okubo, 1970; Weiss, 1991). Spatial domains with  $OW(x, t) < 0$  (rotation prevailing over strain) are generally considered vortical. The  $OW$  parameter is not objective (the vorticity term will change under rotations), and hence no objective threshold level can be defined for this scalar field to identify vortices unambiguously. This ambiguity significantly impacts the overall number and geometry of the vortical structures inferred from the  $OW$  parameter (Appendix E). Among other applications,  $OW$  has been used to study eddies in the Gulf of Alaska (Henson and Thomas, 2008), in the Mediterranean Sea (Isern-Fontanet et al., 2006, 2004, 2003), in the Tasman Sea (Vaughan et al., 2006), and in the global ocean (Chelton et al., 2007).

In Fig. 3, we show elliptic OECSs with the highest persistence metric  $\Theta_\gamma$  for each vortical region, on a surface representing the negative  $OW$  parameter. The plane of the figure also shows the level curves of the  $OW$  parameter. The black numbers in Fig. 3 label the different vortical structures, while the magenta numbers classify them in decreasing order of  $\Theta_\gamma$ . We find elliptic OECSs in locations of the flow where the  $OW$  parameter is close to zero and hence signals no vortices (see, e.g.,  $E\#7$ ,  $E\#8$ ,  $E\#18$ ). In contrast, close to the tip of Africa,  $OW$  signals several strong vortical regions, even though we only detect two belts of elliptic OECSs ( $E\#6$ ,  $E\#16$ ).

To assess these discrepancies between the  $OW$  parameter and our persistence metric  $\Theta_\gamma$ , we compare the coherence strength suggested by  $\Theta_\gamma$  to the actual lifetime of Lagrangian vortices

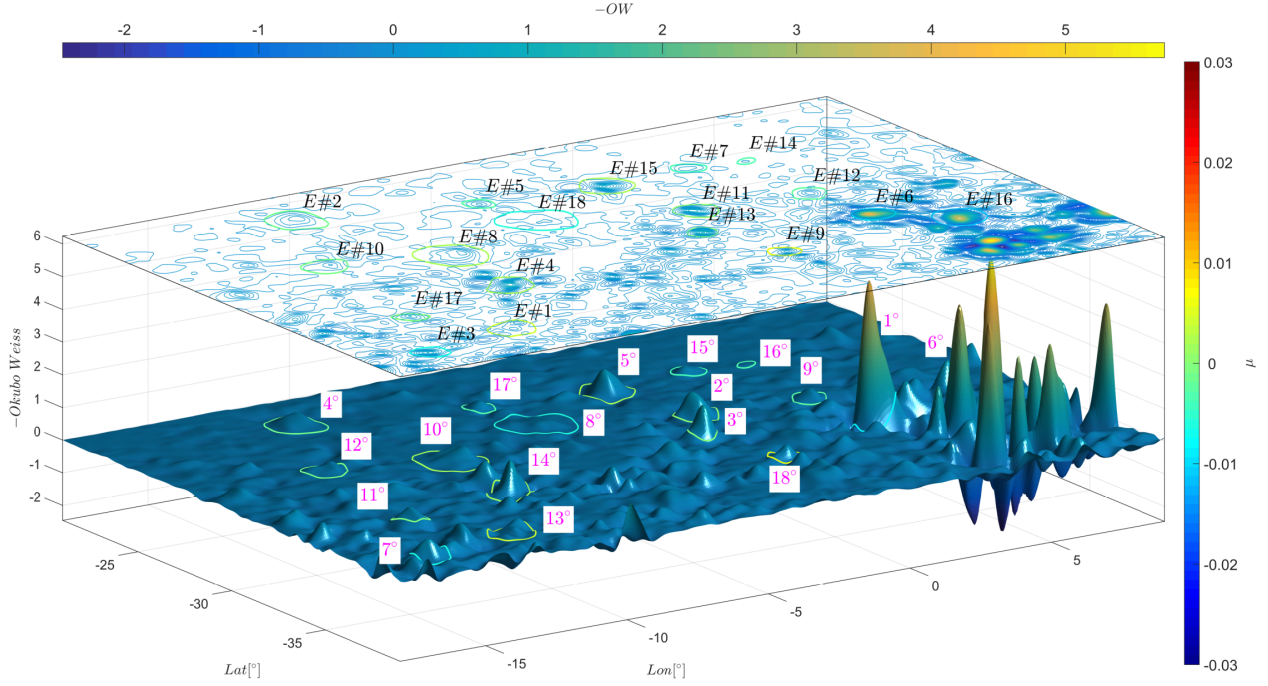


Figure 3: Elliptic OECSs with the highest persistence metric  $\Theta_\gamma$  on a surface representing the negative OW parameter (horizontal colorbar or z-axis). The color of Elliptic OECSs represents the corresponding stretching-rate value  $\mu$  (right colorbar). Black numbers identify different vortical regions detected by elliptic OECSs. In magenta, the classification of the most persistent vortical regions in decreasing order of  $\Theta_\gamma$ .

computed over a time window of four months with initial time  $t = 24$  November 2006. We compute the Lagrangian lifetime of elliptic OECS's as the maximum integration time for which coherent (i.e., non-filamenting) Lagrangian vortices in the sense of Haller and Beron-Vera (2013) exist nearby. To do so, we use the following discrete set of integration times: [7, 15, 30, 60, 90, 120] days. The Lagrangian lifetime of an elliptic OECSs is then the largest integration time from this sequence that still gives a nearby coherent Lagrangian eddy. We consider a Lagrangian eddy to be in the vicinity of an elliptic OECSs if it is contained within a circle of radius  $3^\circ$  ( $\sim 1.5$  times the radius of a mesoscale eddy) centered at the elliptic OECSs.

Figure 4a shows the  $\Theta_\gamma$  values (blue) associated with each vortical region ( $E\#i$ ) in descending order of  $\Theta_\gamma$ . Figures 4b-d, in contrast, show alternative instantaneous metrics, such as the average of  $-OW$ ,  $|\nabla PV|$  and  $|PV|$ , respectively, within the elliptic OECSs shown in Fig. 3. For this dataset, we compute  $PV$  as in Early et al. (2011). The actual Lagrangian lifetime of the underlying vortical regions is shown in red in all the plots, along with its correlations with the different instantaneous metrics.

The instantaneous persistence metric  $\Theta_\gamma$  shows a distinct correlation ( $\rho \approx 0.7$ ) with the lifetime of long-lived Lagrangian eddies in our study domain. This includes eddies #6, #11, #13, #15, #18, #8, #23 and #3, previously identified as exceptionally coherent Lagrangian eddy regions in Haller and Beron-Vera (2013) and Karrasch et al. (2015). Figure 4a shows that out of the ten elliptic OECSs with the highest  $\Theta_\gamma$  values, eight are long-lived Lagrangian vortices.

At the same time, Figs. 4b-d, reveal weak predictive power for other instantaneous Eulerian diagnostics, each of which has significantly lower correlation with the Lagrangian lifetime of eddies. Figures 4b-c show that long-lived mesoscale eddies, such as  $E\#2$  and  $E\#18$ , have surprisingly weak signatures in the  $OW$  and  $|\nabla PV|$  fields, while the vortex #16, which has a relatively low Lagrangian lifetime, has the strongest signature in these two fields. The correlation coefficients of these diag-

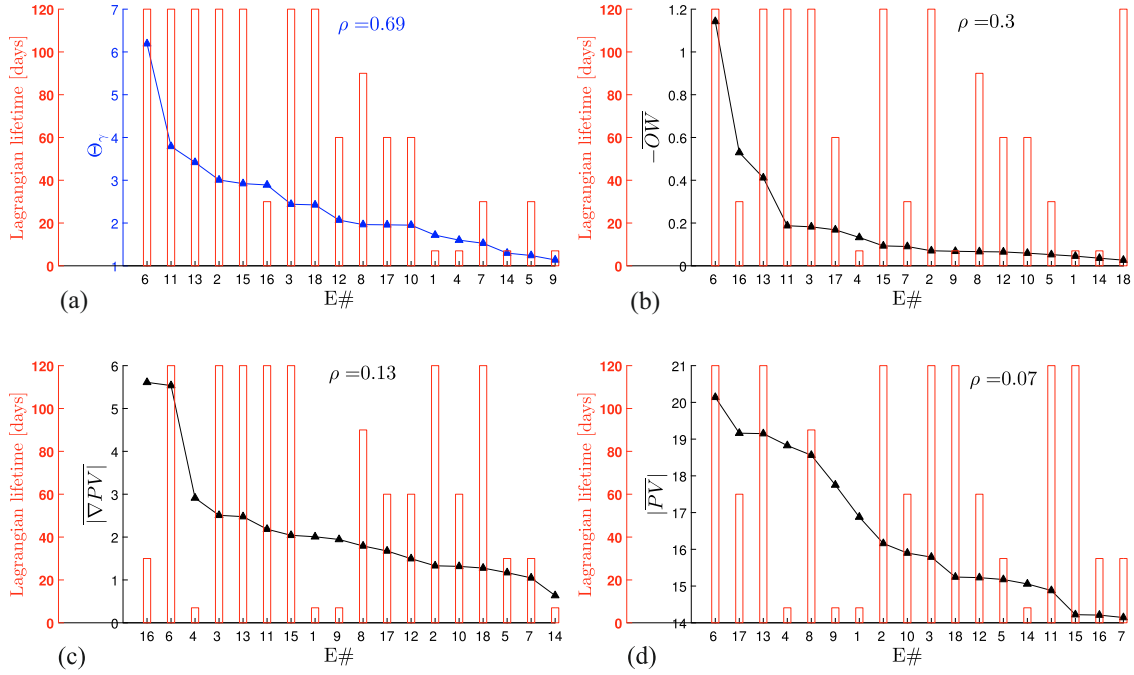


Figure 4: (a) Values of the persistence metric  $\Theta_\gamma$  (blue) for the different vortical regions identified by elliptic OECSs compared with their Lagrangian lifetime (red). (b-d) Spatial average of  $-OW$ ,  $|\nabla PV|$  and  $|PV|$  within elliptic OECSs compared with their Lagrangian lifetime (red). The parameter  $\rho$  indicates the correlation coefficient between the instantaneous prediction given by each metric and the actual Lagrangian lifetime of the underlying vortical region.

nostics would be even lower if the candidate vortical regions were identified from the usual ad hoc threshold values for these methods, instead of elliptic OECSs. Indeed, note that within all the vortical regions in the southeast of the domain signaled by  $OW$ , only one ( $E\#6$ ) predicts correctly a long-lived mesoscale eddy.

Regions of high  $PV$  gradient are also frequently used as indicators of instantaneous ellipticity in unsteady fluid flows. Accordingly, in Appendix E, we plot the Elliptic OECSs of Fig. 3 again over the  $|\nabla PV|$  scalar field. Similarly to the the  $OW$ -criterion, the  $|\nabla PV|$  diagnostic highlights regions where no long-lived Lagrangian eddies are present, while it misses regions where such eddies are known to be present.

One may alternatively compute the Lagrangian lifetime of eddies from other objective elliptic LCS detection methods, such as the Polar Rotation Angle (PRA) defined by Farazmand and Haller (2016) or the Lagrangian-averaged vorticity deviation (LAVD) introduced by Haller et al. (2016). The results (not shown here) obtained in this fashion are close to those in Fig. 4.

## 7 Conclusions

We have introduced a frame-invariant, non-dimensional metric to assess the ability of elliptic objective Eulerian coherent structures (OECS) to identify vortical regions with sustained material coherence. Our metric  $\Theta_\gamma$  is the ratio between a rotational coherence measure of the vortex and the material leakage out of the vortex.

We have tested the  $\Theta_\gamma$  metric on satellite-derived ocean velocity data, where we found that Elliptic OECSs with high  $\Theta_\gamma$  values tend to forecast the exceptionally coherent Lagrangian vortices found in Haller and Beron-Vera (2013) with high probability. To our knowledge, this is the first Eulerian eddy census method that is shown to display a clear correlation with the actual lifetime of

nearby Lagrangian vortices. In contrast, we have found other available Eulerian vortex diagnostics to show a distinct lack of correlation with long-term Lagrangian coherence. This is perhaps unsurprising because none of them is non-dimensional or objective, and none of them is inferred from the infinitesimally short-time limit of a mathematically exact Lagrangian coherence criterion. The lack of correlation of classic Eulerian vortex diagnostics with Lagrangian eddy lifetimes is consistent with the findings of Beron-Vera et al. (2013) and Wang et al. (2016), who show that these diagnostics overestimate the number of materially coherent vortices significantly.

Our proposed vortex persistence metric is purely kinematic, and hence offers a model-independent instantaneous forecasting tool. This tool is free from kinetic assumptions, such as conservation or near-conservation of vorticity or potential vorticity.

Based on the results presented here, we expect our approach to be useful in real-time transport predictions, environmental decision making and hazard assessment. The purpose of this study has been to demonstrate the predictive power of the proposed persistence metric. A more detailed statistical analysis is planned for future work.

## Appendix A Material flux through elliptic OECSs

Here we derive a formula for the instantaneous material flux through an elliptic OECS  $\gamma(t)$ , whose arclength parametrization is denoted by  $x : s \mapsto x(s)$ , with  $s \in [0, \sigma] \subset \mathbb{R}$ . The closed curve  $\gamma(t)$  is a limit cycle of (2), parametrized by  $s$ , that depends smoothly on the time  $t$ . We first observe that  $\gamma(t + \epsilon\Delta t)$  persists for small  $\epsilon\Delta t$ . This is guaranteed by the structural stability of limit cycles of (2) together with the smoothness of the underlying flow map. For small enough  $\epsilon\Delta t$ , therefore there exists a nearby elliptic OECS,  $\gamma(t + \epsilon\Delta t)$ , that is a smooth deformation of  $\gamma(t)$ .

Specifically, we can locally represent the perturbed limit cycle as

$$\begin{aligned} x(s, t + \epsilon\Delta t) &= x(s, t) + g(s, t; \epsilon\Delta t)\chi^\perp(x(s, t), t) \\ &= x(s, t) + \epsilon\Delta t g_1(s, t)\chi^\perp(s, t) + \mathcal{O}((\epsilon\Delta t)^2), \end{aligned} \quad (11)$$

where,  $g$  and  $g_1$  are two smooth scalar functions, and  $\chi^\perp(x(s, t), t)$  is the local normal to the limit cycle at the point  $x(s, t) \in \gamma(t)$ . (For notational simplicity we have used  $\chi$  instead of  $\chi_\mu^\pm$ ). The period of the perturbed limit cycle is of the form  $\sigma_\epsilon = \sigma + \epsilon\sigma_1 + \mathcal{O}(\epsilon^2)$ , leading to the periodicity condition

$$x(0, t + \epsilon\Delta t) = x(\sigma_\epsilon, t + \epsilon\Delta t).$$

Taylor expanding this expression with respect to  $\epsilon$  and comparing the  $\mathcal{O}(\epsilon)$  terms gives

$$\dot{x}(\sigma, t) = \dot{x}(0, t) - \chi(x(\sigma, t), t) \frac{\sigma_1}{\Delta t}, \quad (12)$$

where the dot denotes the derivative with respect to  $t$ . This relation shows that the difference between the perturbation to  $\gamma(t)$  at  $s = 0$  and at  $s = \sigma$ , should be in the direction tangential to the limit cycle  $\gamma(t)$  in order to ensure its persistence as a  $\mathcal{C}^1$  closed curve.

In order to compute the term  $\dot{x}(s, t)$  (in equation (3)), as well as the unknown quantities in (12), we write the equation of variations for the ODE (2) with respect to changes in the parameter  $t$ , leading to

$$(\dot{x}(s, t))' = \nabla\chi(x(s, t), t)\dot{x}(s, t) + \partial_t\chi(x(s, t), t), \quad (13)$$

where the prime denotes the derivative with respect to the parameter  $s$ . Equation (13) is a non-autonomous linear ODE for  $\dot{x}(s, t)$ . In the classic theory of dependence of solutions on parameters,  $\dot{x}(0, t)$  is generally zero since initial conditions do not depend on the parameters. In the present case, however, the initial condition,  $x(0, t)$  does depend on  $t$ . This dependence determines where the limit cycle is and how it deforms as  $t$  varies. We rewrite the ODE (13) using the following shorthand notation:

$$y'(s) = A(s)y(s) + c(s), \quad (14)$$

where

$$y(s) = \dot{x}(s, t), \quad A(s) = \nabla\chi(x(s, t), t), \quad c(s) = \partial_t\chi(x(s, t), t), \quad (15)$$

with the time argument  $t$  suppressed in  $y$ ,  $A$  and  $c$  for brevity.

Note that  $y(s) = \chi(x(s, t), t)$  is a solution to the homogeneous part of (14). As in Haller and Iacono (2003), we solve (14) explicitly in the basis  $[\chi(x(s, t), t), \chi^\perp(x(s, t), t)]$ . With the change of coordinates

$$y(s) = T(s)z(s), \quad T(s) = [\chi(x(s, t), t), \chi^\perp(x(s, t), t)], \quad (16)$$

(14) can be written as

$$z'(s) = \tilde{A}(s)z(s) + \tilde{c}(s). \quad (17)$$

Substituting the change of coordinates (16) into (14) gives

$$T'(s)z(s) + T(s)z'(s) = A(s)T(s)z(s) + c(s). \quad (18)$$

Since  $T(s) \in SO(2)$ , equation (18) can be written as

$$z'(s) = [T^\top(s)A(s)T(s) - T^\top(s)T'(s)]z(s) + T^\top(s)c(s). \quad (19)$$

Using equations (15-16), we can write  $T^\top(s)A(s)T(s)$  and  $T^\top(s)T'(s)$  as

$$T^\top(s)A(s)T(s) = \begin{bmatrix} \langle \chi, \nabla \chi \chi \rangle & \langle \chi, \nabla \chi \chi^\perp \rangle \\ \langle \chi^\perp, \nabla \chi \chi \rangle & \langle \chi^\perp, \nabla \chi \chi^\perp \rangle \end{bmatrix}, \quad (20)$$

$$T^\top(s)T'(s) = \begin{bmatrix} \langle \chi, \nabla \chi \chi \rangle & \langle \chi, R \nabla \chi \chi \rangle \\ \langle \chi^\perp, \nabla \chi \chi \rangle & \langle \chi^\perp, R \nabla \chi \chi \rangle \end{bmatrix}. \quad (21)$$

Differentiating the identity  $\langle \chi, \chi \rangle = 1$  with respect to  $x$ , we obtain the following relations

$$\begin{aligned} (\nabla \chi)^\top \chi &= 0, & \langle \chi, (\nabla \chi)^\top \chi \rangle &= 0, \\ \langle \chi, \nabla \chi \chi \rangle &= 0, & \nabla \chi \chi &\perp \chi, \\ \langle \chi^\perp, \nabla \chi \chi \rangle &= \kappa, & R \nabla \chi \chi &= -\kappa \chi, \end{aligned} \quad (22)$$

where  $\kappa$  denotes the pointwise scalar curvature along the elliptic OECS with respect to the normal vector defined as  $\chi^\perp = R\chi$ . Substituting (20-22) into (19) leads to

$$\tilde{A}(s) = [T^\top(s)A(s)T(s) - T^\top(s)T'(s)] = \begin{bmatrix} 0 & \kappa(s) \\ 0 & \langle \chi^\perp, \nabla \chi \chi^\perp \rangle \end{bmatrix}.$$

The invariance property of the trace of a matrix under orthonormal transformations implies that  $Tr(\nabla \chi) = Tr(T^\top \nabla \chi T)$ . Recalling that  $A = \nabla \chi$ , and using equation (20) and equation (22), we obtain

$$\begin{aligned} \nabla \cdot \chi &= Tr(\nabla \chi) \\ &= Tr(T^\top \nabla \chi T) \\ &= \langle \chi, \nabla \chi \chi \rangle + \langle \chi^\perp, \nabla \chi \chi^\perp \rangle \\ &= \langle \chi^\perp, \nabla \chi \chi^\perp \rangle, \end{aligned}$$

leading to the final form of  $\tilde{A}(s)$ :

$$\tilde{A}(s) = \begin{bmatrix} 0 & \kappa(x(s, t), t) \\ 0 & \nabla \cdot \chi(x(s, t), t) \end{bmatrix}. \quad (23)$$

Now we derive a simplified expression for the forcing term of the ODE (17), i.e., for

$$\tilde{c}(s) = T^\top(s)c(s) = \begin{bmatrix} \langle \chi, \partial_t \chi \rangle \\ \langle \chi^\perp, \partial_t \chi \rangle \end{bmatrix}. \quad (24)$$

To compute  $\partial_t \chi$ , we take the partial derivative of the implicit ODE defining elliptic OECSs with respect to  $t$  to obtain

$$\partial_t \langle \chi(x(s, t), t), [S(r, t) - \mu I] \chi(x(s, t), t) \rangle = 0. \quad (25)$$

Dropping the arguments, we find equation (25) equivalent to

$$\langle \chi, S \partial_t \chi \rangle = -\frac{\langle \chi, \partial_t S \chi \rangle}{2}. \quad (26)$$



Since the direction field  $\chi$  is normalized, we have  $\partial_t \chi(x, t) \perp \chi(x, t)$ , and hence we can write

$$\partial_t \chi(x, t) = \psi(x, t) \chi^\perp(x, t), \quad \psi(x, t) \in \mathbb{R}. \quad (27)$$

Substituting (27) into (26) leads to

$$\psi(x(s, t), t) = -\frac{\langle \chi, \partial_t S \chi \rangle}{2 \langle \chi, S \chi^\perp \rangle}, \quad (28)$$

which is always defined in the domain  $U_\mu$ , unless  $\chi \equiv e_i, i = 1, 2$ , in which case  $\langle e_i, S e_i^\perp \rangle = 0$ .

We are interested in evaluating the instantaneous material flux through elliptic OECSs. Along these curves, the constant instantaneous stretching rate  $\mu$  is approximately zero, and hence the  $\chi_\mu^\pm$  directions are far from the  $e_i$  directions. Specifically, for incompressible flows, the directions  $\chi_0^\pm$  exactly bisect the  $e_i$  directions. Therefore, equation (28) is always well-defined on elliptic OECSs. Substituting (27) and (28) into (24) leads to

$$\tilde{c}(s) = \begin{bmatrix} 0 \\ \psi(x(s, t), t) \end{bmatrix}, \quad (29)$$

as in (6).

Using the variation of constants formula (see e.g., Arnold (1973)), we can write the solution of (17) as

$$\begin{aligned} z(s) &= \Phi_0^s z(0) + \Phi_0^s \int_0^s (\Phi_0^\vartheta)^{-1} \tilde{c}(\vartheta) d\vartheta \\ &= \Phi_0^s z(0) + \Pi(s), \end{aligned}$$

with  $\Phi_0^s$  being the normalized fundamental matrix solution to the homogeneous problem

$$z'(s) = \tilde{A}(s) z(s). \quad (30)$$

By direct integration of (30) we obtain

$$\Phi_0^s = \begin{bmatrix} 1 & \int_0^s e^{\int_0^\vartheta \nabla \cdot \chi_\mu^\pm(x(\vartheta, t), t) d\vartheta} \kappa(x(\vartheta, t)) d\vartheta \\ 0 & e^{\int_0^s \nabla \cdot \chi_\mu^\pm(x(\vartheta, t), t) d\vartheta} \end{bmatrix},$$

as in (5).

Once this fundamental matrix solution is computed, the only missing quantity in (4) is the initial condition  $z(0)$ . To obtain that, we rewrite (12) in the  $z$  coordinates. This, together with (4), leads to the system

$$\begin{cases} z(\sigma) = z(0) - d \frac{\sigma_1}{\Delta t}, & d := [0, 1]^\top \\ z(\sigma) = \Phi_0^\sigma z(0) + \Pi(\sigma). \end{cases} \quad (31)$$

Although this system of equations is undetermined ( $z(\sigma)$ ,  $z(0)$  and  $\sigma_1$  are unknown), it is sufficient to determine the component of  $z(0)$  along the  $\chi^\perp$  direction,  $z^\perp(0)$ . Substituting (4) and (5) into (31), we obtain

$$\begin{bmatrix} 0 & \int_0^\sigma e^{\int_0^y \nabla \cdot \chi_\mu^\pm(x(\vartheta, t), t) d\vartheta} \kappa(x(y, t)) dy \\ 0 & e^{\int_0^\sigma \nabla \cdot \chi_\mu^\pm(x(\vartheta, t), t) d\vartheta} - 1 \end{bmatrix} \begin{bmatrix} z^\parallel(0) \\ z^\perp(0) \end{bmatrix} = - \begin{bmatrix} \Pi^\parallel(\sigma) \\ \Pi^\perp(\sigma) \end{bmatrix} - \begin{bmatrix} 1 \\ 0 \end{bmatrix} \frac{\sigma_1}{\Delta t},$$

where,  $e^{\int_0^\sigma \nabla \cdot \chi_\mu^\pm(x(\vartheta, t), t) d\vartheta} = \rho_1 \rho_2 = \rho_2$ , with  $\rho_1$  and  $\rho_2$  denoting the Floquet multipliers (Guckenheimer and Holmes, 1983) of the  $\sigma$ -periodic limit cycle  $\gamma$  of the ODE (2). Solving this system, we obtain

$$\begin{cases} z^\perp(0) = \frac{\Pi^\perp(\sigma)}{1 - \rho_2} \\ \sigma_1 = \Delta t \left( \Pi^\parallel(\sigma) + z^\perp(0) \int_0^\sigma e^{\int_0^y \nabla \cdot \chi_\mu^\pm(x(\vartheta, t), t) d\vartheta} \kappa(x(y, t)) dy \right), \end{cases} \quad (32)$$

where the first equation is the same as equation (7). The equations in (32) are independent of the value of  $z^{\parallel}(0)$  due to the invariance of material flux under a shift of the parameter  $s$ . The hyperbolic nature of limit cycles ensures that  $\rho_1\rho_2 = \rho_2 \neq 1$ , and thus, both expressions in (32) are well-defined on elliptic OECSs. Observe that the denominator  $(1 - \rho_2)$  is equal to the slope of the Poincaré return map along  $\gamma$ , as shown in Perko (1990). The first equation of (32) is the only component of  $z(0)$  needed for the computation of the instantaneous material flux  $\varphi_{\gamma(t)}$ .

Although  $\sigma_1$  is not strictly necessary for computing  $\varphi_{\gamma(t)}$ , it gives the  $\mathcal{O}(\epsilon)$  variation of the period  $\sigma_\epsilon$  of to the deformed elliptic OECSs, as the parameter  $t$  is perturbed to  $t_\epsilon = t + \epsilon\Delta t$ .

## Appendix B Objectivity of the persistence metric

Here we show that the non-dimensional metric  $\Theta_\gamma(t)$  is objective i.e., invariant under all coordinate changes of the form

$$x = Q(t)\tilde{x} + b(t), \quad (33)$$

where  $Q(t) \in SO(2)$  and  $b(t) \in \mathbb{R}^2$  are smooth functions of time. Since the  $\Theta_\gamma(t)$  is a scalar quantity, in order for it to be objective Truesdell and Noll (2004), at every point it must have the same value independent of the actual coordinates chosen,  $x$  or  $\tilde{x}$ , as long as they are linked by equation (33). To see this, we check objectivity separately for the numerator and denominator of (10).

The spin tensor  $W$  introduced in (1) is well known to be non-objective Truesdell and Noll (2004), as it transforms as

$$\tilde{W} = Q^\top W Q - Q^\top \dot{Q}.$$

Correspondingly, the plane-normal component  $\omega$  of the vorticity transforms under (33) as

$$\tilde{\omega} = \omega - \omega_Q,$$

where,  $\omega_Q$  is such that  $Q^\top \dot{Q} = \omega_Q R$ . The deviation of the vorticity from its spatial mean transforms as

$$\begin{aligned} \tilde{\omega} - \bar{\tilde{\omega}} &= \omega - \omega_Q - \frac{1}{A_{\partial U}} \int_{A_{\partial U}} (\omega - \omega_Q) dA \\ &= \omega - \frac{1}{A_{\partial U}} \int_{A_{\partial U}} \omega dA = \omega - \bar{\omega}, \end{aligned} \quad (34)$$

where, in the second line we used the fact that the domain  $U$  is time independent and  $\omega_Q$  is space independent. Formula (34) proves the objectivity of  $\omega_{\gamma(t)}$  defined in (8).

To show the objectivity of the relative material leakage defined in (9), we rewrite the pointwise material flux density (3) in the simplified form:

$$\varphi = \langle \dot{x}_{a1} - \dot{x}_{a2}, \Delta x \rangle, \quad (35)$$

where,  $\dot{x}_{a1}$  and  $\dot{x}_{a2}$  represent two general velocity vectors which have the same base point  $x_a$ , and  $\Delta x = x_a - x_b$  is a simple distance vector between two points. Representing these quantities in the  $\tilde{x}$  frame, we obtain

$$\begin{aligned} \tilde{\dot{x}}_{ai} &= Q^\top \dot{x}_{ai} - Q^\top \dot{Q} \tilde{x}_{ai} - Q^\top \dot{b}, \quad i = 1, 2, \\ \tilde{\Delta x} &= Q^\top \Delta x, \end{aligned}$$

that, together with (35) leads to

$$\begin{aligned} \tilde{\varphi} &= \langle -Q^\top \dot{Q}(\tilde{x}_{a1} - \tilde{x}_{a2}) + Q^\top(\dot{x}_{a1} - \dot{x}_{a2}), Q^\top \Delta x \rangle, \\ &= \langle Q^\top(\dot{x}_{a1} - \dot{x}_{a2}), Q^\top \Delta x \rangle, \\ &= \varphi, \end{aligned}$$

where, we used the properties of  $Q$  and that  $\tilde{x}_{a1} = \tilde{x}_{a2} = \tilde{x}_a$  in any coordinate frame since they represent the same base point for the two velocity vectors involved in the material flux computation. We have therefore shown that  $\omega_\gamma$  and  $\Gamma_\gamma$  are both objective quantities, and hence so is the vortex persistence metric,  $\Theta_\gamma$ , introduced in Definition 3.

## Appendix C Numerical steps for the computation of elliptic OECSs and $\Theta_\gamma$

---

**Algorithm 1** Compute elliptic OECSs (Serra and Haller, 2016)

---

**Input:** A 2-dimensional velocity field.

1. Compute the rate-of-strain tensor  $S(x, t) = \frac{1}{2} \left( \nabla v(x, t) + [\nabla v(x, t)]^T \right)$  at the current time  $t$  on a rectangular grid over the  $(x_1, x_2)$  coordinates.
2. Detect the singularities of  $S$  as common, transverse zeros of  $S_{11}(\cdot, t) - S_{22}(\cdot, t)$  and  $S_{12}(\cdot, t)$ , with  $S_{ij}$  denoting the entry of  $S$  at row  $i$  and column  $j$ .
3. Determine the type of the singularity (trisector or wedge) as described in Farazmand et al. (2014).
4. Locate isolated wedge-type pairs of singularities and place the Poincaré sections at their midpoint.
5. Compute the eigenvalue fields  $s_1(x, t) < s_2(x, t)$  and the associated unit eigenvector fields  $e_i(x, t)$  of  $S(x, t)$  for  $i = 1, 2$ .
6. Compute the vector field  $\chi_\mu^\pm(r(s)) = \sqrt{\frac{s_2 - \mu}{s_2 - s_1}} e_1 \pm \sqrt{\frac{\mu - s_1}{s_2 - s_1}} e_2$  for different values of stretching rate  $\mu$ , remaining in the range  $\mu \approx 0$ .
7. Use the Poincaré sections as sets of initial conditions in the computation of limit cycles of

$$x'(s) = \text{sign} \left\langle \chi_\mu^\pm(x(s)), \frac{dx(s-\Delta)}{ds} \right\rangle \chi_\mu^\pm(x(s)),$$

where the factor multiplying  $\chi_\mu^\pm(x(s), t)$  removes potential orientation discontinuities in the direction field  $\chi_\mu^\pm(x(s), t)$  away from singularities, and  $\Delta$  denotes the integration step in the independent variable  $s$ .

**Output:** Elliptic OECSs, related  $\chi_\mu^\pm$  tangent field and rate of strain tensor field  $(S(x, t))$ .

---

---

**Algorithm 2** Compute the persistence metric for each elliptic OECS

---

**Input:** A 2-dimensional velocity field, elliptic OECSs, related  $\chi_\mu^\pm$  tangent fields and  $S(x, t)$ .

1. For each elliptic OECS  $\gamma$ , compute the rotational coherence  $\omega_\gamma(t)$ .

a) Compute vorticity scalar field  $\omega(x, t)$ .

b) Compute  $\omega_\gamma(t)$  as:

$$\omega_\gamma(t) = \frac{|\int_{A_{\gamma(t)}} [\omega(x, t) - \bar{\omega}(t)] dA|}{A_{\gamma(t)}},$$

where  $A_{\gamma(t)}$  is the area enclosed by  $\gamma(t)$  and  $\bar{\omega}(t) = \frac{\int_{A_{\partial U}} \omega(x, t) dA}{A_{\partial U}}$ .

2. For each elliptic OECS,  $\gamma$ , compute the relative material leakage,  $\Gamma_\gamma(t)$ :

a) Compute the curvature scalar  $\kappa$  and the divergence  $\nabla \cdot \chi$  of the  $\chi_\mu^\pm$  tangent field along elliptic OECSs.

b) Compute  $\partial_t S$  along elliptic OECSs using a backward finite differencing scheme.

c) Using equations (3-7), compute  $\Gamma_\gamma(t)$  as

$$\Gamma_\gamma(t) = \frac{\oint_{\gamma(t)} |\varphi(x(s, t), t)| ds}{A_{\gamma(t)}}.$$

3. For each elliptic OECS,  $\gamma$ , compute  $\Theta_\gamma(t) = \frac{\omega_\gamma(t)}{\Gamma_\gamma(t)}$ .

4. Within each elliptic OECSs belt (candidate eddy region), select the one with the maximal  $\Theta_\gamma(t)$ .

**Output:** List of coexisting elliptic OECSs with their correspondent metric value  $\Theta_\gamma(t)$ .

---

Here we propose a systematic way to monitor the accuracy of numerical differentiation involved in equations (5-6). Specifically, equation (5) requires spatial differentiation for the computation of  $\nabla \cdot \chi$  (step (ii)a), while equation (6) requires differentiation in time to compute  $\partial_t S$  (step (ii)b).

To select the appropriate stepsize for the spatial differentiation of the  $\chi$  field, we turn the relation  $(\nabla \chi)^\top \chi = 0$ , shown in Appendix A, into the scalar equation  $\langle \chi, \nabla \chi (\nabla \chi)^\top \chi \rangle = 0$ . The deviation of  $\langle \chi, \nabla \chi (\nabla \chi)^\top \chi \rangle$  from zero allows to quantitatively monitor the entity of the error due to spatial differentiation in the material flux computation. For instance, a complex geometry of the elliptic OECS would require a finer grid for the accurate computation of  $\nabla \chi$ . This refinement, however, is needed only to handle sharp changes in the elliptic OECSs, which are signaled by high values of the curvature scalar  $\kappa$ . Therefore, it is possible to fix a desired maximum allowable deviation of  $\langle \chi, \nabla \chi (\nabla \chi)^\top \chi \rangle$  from zero and select the spatial resolution accordingly.

In a similar fashion, we monitor also the accuracy of numerical finite differencing in the time direction used to compute  $\partial_t S$  in (6). Since the direction field  $\chi$  is normalized, differentiating the identity  $\langle \chi_\mu, \chi_\mu \rangle = 1$  with respect to time leads to  $\partial_t \chi_\mu \perp \chi_\mu$ . Monitoring the deviation of  $|\langle \frac{\partial_t \chi_\mu}{|\partial_t \chi_\mu|}, \chi_\mu \rangle|$  from zero allows a systematic assessment of the appropriate time step required to compute  $\partial_t S$ .

The quantities  $\langle \chi, \nabla \chi (\nabla \chi)^\top \chi \rangle$  and  $|\langle \frac{\partial_t \chi_\mu}{|\partial_t \chi_\mu|}, \chi_\mu \rangle|$  play the role of numerical reliability parameters and allow us to compute the material flux through any elliptic OECS in an efficient and accurate fashion.

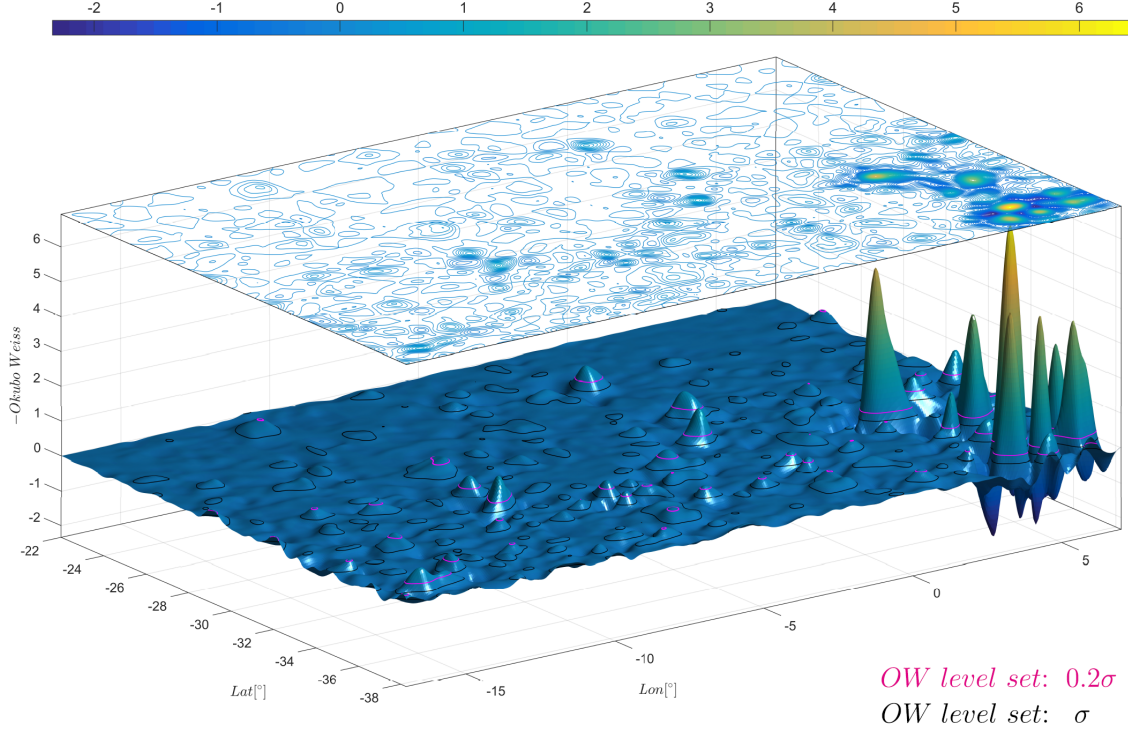


Figure 5:  $OW$  parameter and two specified level sets corresponding to  $OW = 0.2\sigma$  (magenta) and  $OW = \sigma$  (black) with  $\sigma$  being the  $OW$  spatial standard deviation.

## Appendix D Ocean surface flow dataset

Under the geostrophic assumption, the ocean surface topology measured by satellites plays the role of a stream function for the related surface currents. With  $h$  denoting the sea surface height, the velocity field in longitude-latitude coordinates  $[\phi, \theta]$ , can be expressed as

$$\dot{\phi} = -\frac{g}{R^2 f(\theta) \cos \theta} \partial_{\theta} h(\phi, \theta, t), \quad \text{and} \quad \dot{\theta} = \frac{g}{R^2 f(\theta) \cos \theta} \partial_{\phi} h(\phi, \theta, t),$$

where  $f(\theta) := 2\Omega \sin \theta$  denotes the Coriolis parameter,  $g$  the constant of gravity,  $R$  the mean radius of the earth and  $\Omega$  its mean angular velocity. The velocity field is available at weekly intervals, with a spatial longitude-latitude resolution of  $0.25^\circ$ . For more detail on the data, see Beron-Vera et al. (2013).

## Appendix E Thresholding requirement for common Eulerian diagnostics

Vortex definitions based on scalar fields (e.g.,  $OW$ ) are often ambiguous due to their dependence on ad hoc of thresholding parameters. For the  $OW$ -criterion, this threshold value is typically  $\alpha\sigma$ , with  $\sigma$  being the spatial standard deviation of the  $OW$  parameter, and  $\alpha \in \mathbb{R}$  selected as a problem-dependent constant. Figure 5 shows the  $OW$  level sets for two different values of  $\alpha$ : 0.2 and 1, as suggested in Henson and Thomas (2008) and Koszalka et al. (2009), respectively. Note how the values of  $\alpha$  can significantly change the overall number and geometry of vortices identified.

In Fig. 6, we show the elliptic OECSs with highest vortex persistence metric  $\Theta_{\gamma}$ , shown in Fig. 3, on a scalar field representing the  $|\nabla PV|$  where  $PV$  is computed as in Early et al. (2011).

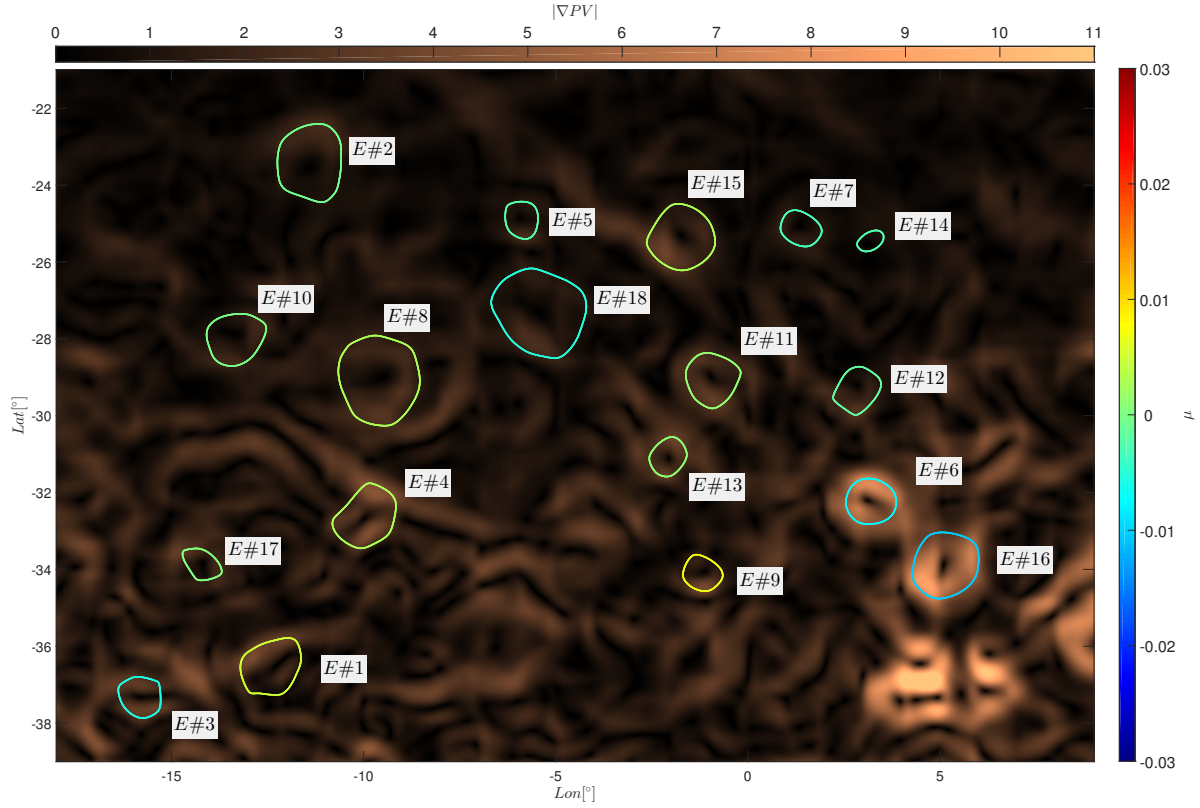


Figure 6: Elliptic OECSs with highest vortex persistence metric  $\Theta_\gamma$ , plotted over  $|\nabla PV|$  (horizontal colorbar). Elliptic OECSs are encoded with a color representing their stretching-rate value  $\mu$  (right colorbar). Black numbers label different vortical regions encircled by elliptic OECSs.

Regions of high  $PV$  gradient are frequently used indicators of instantaneous ellipticity in unsteady fluid flows. In the south-east of the domain ( $[1^\circ E, 7^\circ E]$ ,  $[31^\circ S, 38^\circ S]$ ), although there are several regions of high  $|\nabla PV|$ , only one long-lived Lagrangian eddy is present. At the same time,  $|\nabla PV|$  fails to signal several other regions captured by elliptic OECSs (see e.g., eddies #2, #8, and #18), where long-lived Lagrangian eddies are present. Therefore, a prediction based only on  $|\nabla PV|$ , i.e., choosing an ad hoc threshold parameter to locate vortices instead of using elliptic OECSs, would be even weaker than the one shown in Fig. 4c. A similar conclusion holds for the  $OW$ -criterion, as discussed in section 6.

## References

- V. Arnold. *Ordinary Differential Equations*. MIT Press, Boston, 1973.
- G. K. Batchelor. *An introduction to fluid dynamics*. Cambridge univ. press, 2000.
- L. M. Beal, W. P. M. De Ruijter, A. Biastoch, R. Zahn, and SCOR/WCRP/IAPSO WORKING GROUP. On the role of the Agulhas system in ocean circulation and climate. *Nature*, 472(7344): 429–436, 2011.
- F. J. Beron-Vera, Y. Wang, M. J. Olascoaga, G. J. Goni, and G. Haller. Objective detection of oceanic eddies and the Agulhas leakage. *J. Phys. Oceanogr.*, 43:1426–1438, 2013.
- D. B. Chelton, M. G. Schlax, R. M. Samelson, and R. A. De Szoeke. Global observations of large oceanic eddies. *Geophys. Res. Lett.*, 34, 2007.
- J. J. Early, R. M. Samelson, and D. B. Chelton. The evolution and propagation of quasigeostrophic ocean Eddies\*. *J. Phys. Oceanogr.*, 41:1535–1555, 2011. doi: 10.1175/2011JPO4601.1.
- M. Farazmand and G. Haller. Polar rotation angle identifies elliptic islands in unsteady dynamical systems. *Physica D*, 315:1 – 12, 2016. ISSN 0167-2789. doi: <http://dx.doi.org/10.1016/j.physd.2015.09.007>. URL <http://www.sciencedirect.com/science/article/pii/S0167278915001748>.
- M. Farazmand, D. Blazeviski, and G. Haller. Shearless transport barriers in unsteady two-dimensional flows and maps. *Physica D*, 278:44–57, 2014.
- A. Griffa, A. D. Kirwan, A. J. Mariano, T. Özgökmen, and H. T. Rossby. *Lagrangian analysis and prediction of coastal and ocean dynamics*. Cambridge University Press, 2007.
- J. Guckenheimer and P. Holmes. *Nonlinear oscillations, dynamical systems, and bifurcations of vector fields*, volume 42. Springer Science & Business Media, 1983.
- G. Haller. Lagrangian coherent structures. *Annual Rev. Fluid. Mech.*, 47:137–162, 2015.
- G. Haller and F. J. Beron-Vera. Coherent Lagrangian vortices: the black holes of turbulence. *J. Fluid Mech.*, 731, 9 2013. ISSN 1469-7645. doi: 10.1017/jfm.2013.391. URL [http://journals.cambridge.org/article\\_S0022112013003911](http://journals.cambridge.org/article_S0022112013003911).
- G. Haller and R. Iacono. Stretching, alignment, and shear in slowly varying velocity fields. *Phys. Rev. E*, 68:056304, 2003.
- G. Haller, A. Hadjighasem, M. Farazmand, and F. Huhn. Defining coherent vortices objectively from the vorticity. *J. Fluid Mech.*, 795:136–173, 5 2016. ISSN 1469-7645. doi: 10.1017/jfm.2016.151. URL [http://journals.cambridge.org/article\\_S0022112016001518](http://journals.cambridge.org/article_S0022112016001518).
- S. A. Henson and A. C. Thomas. A census of oceanic anticyclonic eddies in the Gulf of Alaska. *Deep Sea Res. Part I: Oceanogr. Res. Papers*, 55:163–176, 2008.
- J. Isern-Fontanet, E. García-Ladona, and J. Font. Identification of marine eddies from altimetric maps. *J. of Atmosph. and Oceanic Technology*, 20:772–778, 2003.
- J. Isern-Fontanet, J. Font, E. García-Ladona, M. Emelianov, C. Millot, and I. Taupier-Letage. Spatial structure of anticyclonic eddies in the Algerian basin (Mediterranean Sea) analyzed using the Okubo–Weiss parameter. *Deep Sea Res. Part II: Topical Studies in Oceanogr.*, 51:3009–3028, 2004.

- J. Isern-Fontanet, E. García-Ladona, and J. Font. Vortices of the Mediterranean Sea: An altimetric perspective. *J. Phys. Oceanogr.*, 36:87–103, 2006.
- D. Karrasch, F. Huhn, and G. Haller. Automated detection of coherent Lagrangian vortices in two-dimensional unsteady flows. In *Proc. R. Soc. Lond. A.*, volume 471. The Royal Society, 2015.
- I. Koszalka, A. Bracco, J. C. McWilliams, and A. Provenzale. Dynamics of wind-forced coherent anticyclones in the open ocean. *J. Geophys. Res.: Oceans (1978–2012)*, 114, 2009.
- A. Okubo. Horizontal dispersion of floatable particles in the vicinity of velocity singularities such as convergences. In *Deep-Sea Res.*, volume 17, pages 445–454. Elsevier, 1970.
- L. M. Perko. Global families of limit cycles of planar analytic systems. *Trans. of the American Math. Society*, 322:627–656, 1990.
- M. Serra and G. Haller. Objective Eulerian Coherent Structures. *Chaos, (in press)*, 2016.
- C. Truesdell and W. Noll. *The non-linear field theories of mechanics*. Springer, 2004.
- Y Wang, F. J. Beron-Vera, and M. J. Olascoaga. The life cycle of a coherent Lagrangian Agulhas ring. *arXiv preprint arXiv:1601.01560*, 2016.
- D. W. Waugh, E. R. Abraham, and M. M. Bowen. Spatial variations of stirring in the surface ocean: A case study of the Tasman Sea. *J. Phys. Oceanogr.*, 36:526–542, 2006.
- J. Weiss. The dynamics of enstrophy transfer in two-dimensional hydrodynamics. *Physica D*, 48: 273–294, 1991.